12th International Symposium on Turbulence and Shear Flow Phenomena (TSFP12)
Osaka, Japan, July 19–22, 2022

SWEEP EFFECTS ON A CANONICAL SHOCK WAVE/TURBULENT BOUNDARY LAYER INTERACTION

Thomas Bergier(*), Romain Gojon, Jérémie Gressier, Stéphane Jamme and Laurent Joly
ISAE-SUPAERO, University of Toulouse, France
(*)thomas.bergier@isae-supaero.fr

ABSTRACT

This study focuses on the effect of a sweep angle between the upstream mean flow direction and the shock plane normal in a canonical oblique shock wave/boundary layer interaction. We study a configuration based on the experiments of Bo *et al.* (2012): an incident shock impinges on a turbulent boundary layer developing at free stream Mach number $M = 2.7$ and a Reynolds number $Re_\theta = 3200$. The sweep angle is implemented by adding a spanwise velocity component (crossflow) at the inflow and enforcing periodicity conditions on the side boundaries. Several sweep angles are investigated and compared to a canonical unswept case. A viscosity is selected for each case in an effort to keep a constant Re_θ across the whole range of sweep angles. The mean flow structure is analyzed, showing a strongly skewed flow around the separation zone that increases in size compared to a reference unswept case. Pressure loads on the wall surface are also higher for swept cases; and the characteristic low-frequencies of the flow separation also slightly increase.

INTRODUCTION

Shock/boundary layer interaction (SBLI) is a phenomenon commonly found in supersonic airflows. Several different configurations have already been studied (Clemens & Narayanaswamy (2014)) over the last decades among which the interaction of an oblique shock impinging on a turbulent boundary layer (TBL) developing on a flat plate. This setup is known to lead to the formation of a separation bubble, due to the adverse pressure gradient created by the presence of the shock, as well as a "reflected" shock upstream of this bubble. This reflected shock/bubble system exhibits low frequency streamwise oscillations which can be the cause of detrimental pressure and load fluctuations. Efforts have been made to reduce the amplitude of these oscillations using control devices, among which micro-vortex generators. These devices and their impact on impinging SBLI configuration have been the focus of a recent work (Grébert *et al.* (2018)).

Even though SBLI and different control strategies have already been studied , most of these previous works were done on "canonical" setups, *i.e* cases not accounting for potential three-dimensional effects such as curvature of the wall or a sweep angle of the shock plane with respect to the incoming flow. These would however be more representative of a practical configuration of SBLI featuring vertical fins or swept ramps for instance. The objective of the present work is to address this question by investigating the effect of a sweep angle as shown in figure 1 using Large Eddy Simulations (LES).

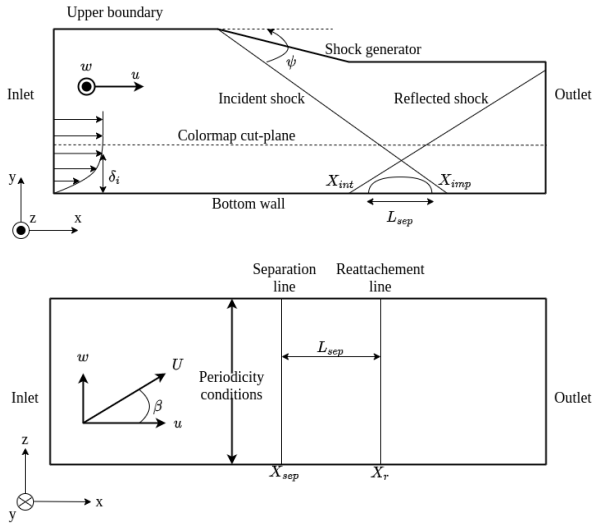

Figure 1: Schematic representation of a swept configuration of SBLI and associated computational domain. Side view (top), top view (bottom).

NUMERICAL SETUP

The present LES were performed with the IC3 solver, which solves the spatially filtered compressible Navier-Stokes equation using, in our case, spectral difference methods applied on an unstructured mesh for the spatial discretization. Spectral difference methods (SD) are based on a polynomial representation of the solution inside the cell and of the numerical flow at the interface between cells (Liu *et al.* (2006)). Moreover, each control volume of the mesh is divided into several "spectral points" (also called "degrees of freedom", or "nDofs") where the solution is given and whose number depends on the order of the scheme used. A 4$^{\text{rd}}$ order spectral scheme is used in the present work for the spatial part, meaning that each control volume (cv) contains 4 spectral points in each direction, giving a total of 64 solution points by cv. The temporal integration uses a 3$^{\text{rd}}$ order Runge-Kutta method and no subgrid scale model is used. In order to deal with discontinuities, we use a limiter specially developed for high-order compact numerical schemes such as SD methods, named SWeP (Spatially Weighted Projections). This limiter is based on a reduction of the order of the polynomial used to describe the solution at the cells affected by discontinuities (Lamouroux *et al.* (2016)).
The size of the computational domain in our simulations corresponds to $L_x \times L_y \times L_z = 59.6\delta_i \times 17.95\delta_i \times 8.54\delta_i$, δ_i being the boundary layer thickness at the inlet of the domain

Table 1: Physical parameters of the simulation

M_∞	T_∞	P_∞	u_∞	ψ
2.7	300 K	101 kPa	937 m/s	30.3°

($\delta_i = 1.12 \times 10^{-3}$m). The grid is uniform along spanwise (z coordinate) and longitudinal (x coordinate) directions, except in the region near the interaction where the longitudinal size of the cells is reduced to better handle the strong adverse pressure gradient. With this meshing strategy, we have $\Delta_x^+ = [11.5; 16.8]$ and $\Delta_z^+ = 10.6$. The grid in the wall-normal direction (y coordinate) is gradually refined towards the bottom wall with $\Delta_y^+ = [0.6; 72.1]$. As we do not use any wall model, this level of precision is needed near the wall to be able to resolve accurately the viscous sub-layer of the boundary layer. The mesh results in $1384 \times 216 \times 260$ nDofs in x, y and z directions respectively, giving a total of around 77.7×10^6 nDofs.

The SBLI configuration selected in this work is the one studied by Grébert *et al.* (2018) and is based on Bo *et al.* (2012) experiments. The physical parameters used in the inlet of the computational domain, as well as the shock features (angle of shock ψ), are summarized in Table 1. Regarding the boundary conditions (see figure 1 for their location), an adiabatic wall is used on the bottom boundary, a symmetry condition is used at the shock generator so that no boundary layer develops here and, on the upper boundary, value of the primitive variables of the flow are imposed. For the outlet, in the supersonic area (outside of the boundary layer) variables are extrapolated. For the subsonic area (inside the boundary layer), the value of static pressure is imposed equal to the mean of the pressure retrieved at the outlet for the supersonic area. At the inlet, the production of turbulence is achieved thanks to a "digital filtering" technique based on a filtering operation applied to statistical data (Touber & Sandham (2009)). It was first introduced by Klein *et al.* (2003) and then modified by Xie & Castro (2008) and Touber & Sandham (2009). This method presents the advantage of not introducing any artificial low-frequency mode, as opposed to recycling or synthetic turbulence techniques. This is important in the case of SBLI as this phenomenon is known for displaying low-frequency dynamics. However, turbulence obtained thanks to digital filtering needs a certain length of development, around [15-20δ_i], to reach a physical state.

RESULTS

The aim of these simulations is to compare the behaviour of the mean flow, as well as the unsteady behaviour of the interaction system for different sweep angles. The sweep angles (β) considered in this work are given in Table 2. The simulations are performed with what is called in the literature "infinite sweep", meaning that sweep is obtained introducing a spanwise (crossflow) velocity component for the incoming flow and using periodic conditions at the spanwise boundaries. Thus, in our computational domain, the shock plane stays the same as in the unswept case but the upstream flow is modified (figure 1). It should be noted that in the flow configuration of a swept shock impinging on a boundary layer, two flow configurations can be observed experimentally regarding the topology of the interaction area depending on the value of the sweep angle (Padmanabhan *et al.* (2021)). For low sweep angles, a cylindrical symmetry is expected, *i.e* separation and reattachment lines are parallel, whereas for higher sweep angles, conical symmetry appears, meaning that the separation and reattachment lines are no longer parallel. As previously mentioned, periodic boundary conditions are imposed in the simulations presented in this work, preventing conical symmetry of the interaction area, and making it irrelevant to study these cases with our current numerical setup. According to Padmanabhan *et al.* (2021), the limit between cylindrical and conical symmetries for their configuration, which is quite close to ours, is 24.7°. This is why we chose to study the range of sweep angles presented in Table 2, all belonging to the cylindrical symmetry. It can also be noted that the Mach number given in Table 2 is the axial Mach number ($M_x = u/c_0$) : the added spanwise velocity component has no influence on the shock itself as its plane is aligned with the spanwise direction and tangential velocity is conserved. Thus, the incident shock features (angle ψ and flow deviation) are the same regardless of the sweep angle.
It should also be noticed that as upstream velocity magnitude is increased to reach the desired sweep angle, the viscosity of the fluid is also increased, with the aim to keep a constant Reynolds number (as well as constant axial Mach number) across our sweep angle range. This can be verified in Table 2 that reports very close values for Re_θ measured at the interaction location between our different cases.

Table 2: Parameters for the different swept case upstream of the interaction.

β (°)	w_∞ (m/s)	μ_∞ (Pa · s)	$Re_\theta(x = X_{int})$	M_x
0	0	4.5×10^{-5}	3371	2.7
15	251.27	4.681×10^{-5}	3367	2.7
20	341.32	4.812×10^{-5}	3381	2.7

Boundary layer validation

Before carrying out the swept SBLI computations, the state of the upstream turbulent boundary layer has to be assessed. Indeed, we have to make sure that the synthetic turbulence created at the inlet has developed well and that it is consistent between our different cases. The turbulent boundary layer characteristics are shown in figure 2 for the different sweep angles and compared to DNS data or correlations from the literature. The value of incompressible friction coefficient Cf_i is obtained thanks to the van Driest II transformation (Van Driest (1956)) :

$$Cf_i = F_c Cf \text{ with } F_c = \frac{T_w/T_\infty - 1}{\arcsin^2 \alpha} \quad \text{and } \alpha = \frac{T_w/T_\infty - 1}{\sqrt{T_w/T_\infty (T_w/T_\infty - 1)}} \tag{1}$$

with T_w the wall temperature. This allow to compare our data, obtained from compressible simulation, with incompressible data or correlations, like Karman-Schoenherr

(KS) or Blasius (BL) (Hopkins & Inouye (1971)) :

$$Cf_{KS} = \frac{1}{17.08\log(Re_{\theta_i})^2 + 25.11\log(Re_{\theta_i}) + 6.012}$$
$$Cf_{BL} = \frac{0.026}{(Re_{\theta_i})^{1/4}}, \quad \text{with } Re_{\theta_i} = \frac{\mu_\infty}{\mu_w} Re_\theta \tag{2}$$

μ_w being the dynamic viscosity at the wall.

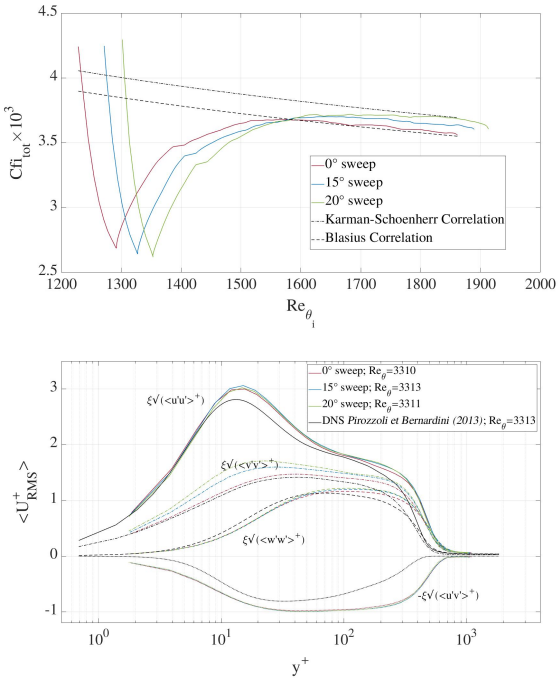

Figure 2: Top : Time and spanwise-averaged incompressible friction coefficient, based on longitudinal and spanwise velocity components (u and w) over the bottom wall, upstream of the interaction. Bottom : Reynolds stress tensor components (spanwise-averaged), values are made dimensionless by taking into account u and w.

The shift in Re_{θ_i} observed on the upper image of figure 2 when the sweep angle increases can be explained by the fact that as β goes up, μ_e increases more than does μ_w (which is obtained from T_w with a power law). The development length of the turbulence can clearly be seen looking at the undershoot of $Cf_{i_{tot}}$ near the inlet of the domain. More downstream, all curves can be found at reasonable Cf_i levels compared to the correlation, and pretty close to each other. On the bottom figure, the Reynolds stress tensor components are globally close to the DNS results. Differences can however be observed, particularly for the $< u'v' >$ component which is overestimated over the whole profile compared to the reference data.

SBLI results and sweep effects

Regarding the SBLI simulations, the mean flow is studied first, especially near the interaction zone. Time-averaged skin friction lines are presented in figure 3, where they are superimposed to a colormap displaying the difference between

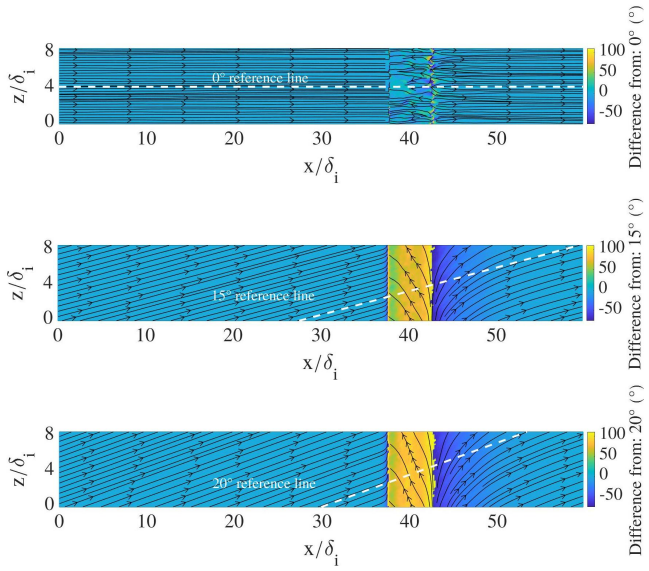

Figure 3: Time-averaged skin-friction lines superimposed to a colormap displaying the gap between the reference angle and the actual computed angle $\arctan(< w > / < u >)$ at the bottom wall. From top to bottom : $\beta = 0°$, $\beta = 15°$, $\beta = 20°$.

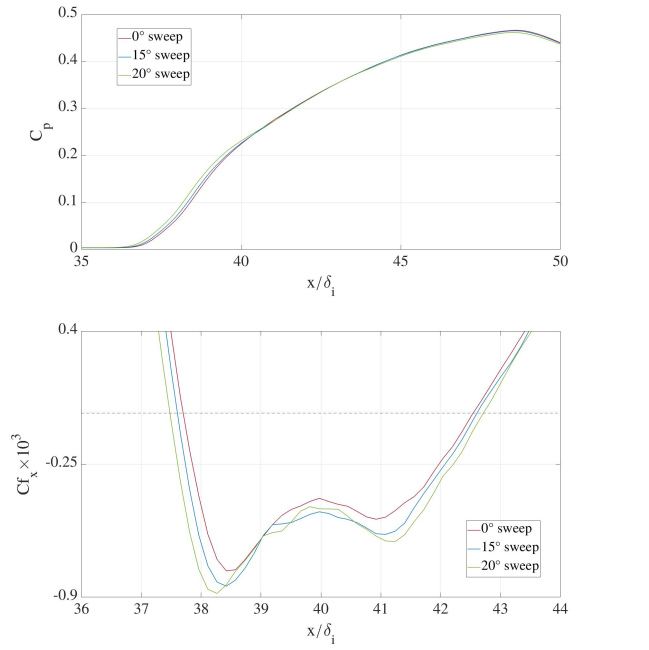

Figure 4: Top : Evolution of $C_p = (P_w - P_\infty)/(\gamma P_\infty M_x^2/2)$, time-averaged pressure coefficient. Bottom : evolution of Cf_x, time-averaged x-wise skin friction coefficient around the separated area. The horizontal dashed line corresponds to $Cf_x = 0$, used to delimit the extent of the separation bubble.

the prescribed sweep angle and the actual angle of the flow with respect to the longitudinal (x-wise) direction. This measure was chosen because it provides a clear visualization of the separated area. This zone seems to grow in size as the sweep angle increases. This observation is comforted by the study of the x-wise skin friction coefficient (defined using the longitudinal component of the wall shear stress) along the bottom wall which shows a greater separated area (zone where $Cf_x < 0$)

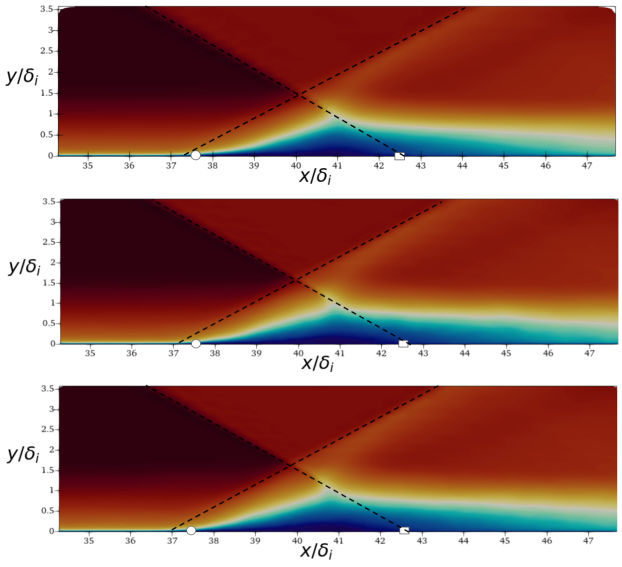

Figure 5: Maps of time-averaged longitudinal velocity. Incident and reflected shocks locations (extrapolated inside the boundary layer) are marked with dashed lines. Mean separation location is located with white circle and mean reattachment point with white square. Scale is the same for the 3 maps and ranges from $u = 0$ to $u = u_\infty$. From top to bottom : $\beta = 0°$, $\beta = 15°$ and $\beta = 20°$.

when the sweep angle increases, as seen in figure 4 (bottom). A possible explanation for this phenomenon, also presented by Larsson *et al.* (2022), is that the wall being adiabatic and the overall Mach number increased by the added swept, the wall temperature at a given longitudinal location is higher for a higher sweep angle. This induces a decreased near-wall density, and thus decreased near-wall inertia, leading to an upstream shift of the separation line. The different separation lengths and wall average temperatures (given for $x = 35\delta_i$, at a location just upstream of the interaction) are specified in Table 3. As it stands, we cannot ensure that temperature alone plays the dominant role in the growing of the separated area. Indeed, a study involving constant wall temperature across the whole sweep angle range would be needed to discriminate the different possible effects (see Larsson *et al.* (2022) for such a study). In addition to the longitudinal size of the separation bubble, one can take an interest in the wall-normal size of said bubble. Figure 5 shows maps of time-averaged longitudinal velocity (u) in the $x-y$ plane around the interaction zone. The separation bubble is found to grow slightly in size as the the sweep angle increases, even if the differences remain very small and are not easy to discriminate on the figure.

In order to investigate the behaviour of the flow away from the wall, we present in figure 6 the streamlines at four y-locations distributed across the thickness of the inlet boundary layer (*i.e.* for $0 < y < \delta_i$) for the the swept cases $\beta = 15°$ and $\beta = 20°$. It can clearly be seen that the flow is highly deviated near the separation and reattachment lines, and that the closer to the wall, the more important the deviation. This leads to a strongly skewed flow around the separation zone, which makes it prone to develop flow instabilities in this region. Further downstream, the flow tends to recover towards the expected post-shock direction, beyond $x/\delta_i = 50$, even though a full recovery is not reached before the end of the computational domain. Figure 7 displays the streamwise evolution of the angle of the flow with respect to the x axis (*i.e.* $\arctan(< w > / < u >)$). The above-mentioned remarks are confirmed by theses curves that also show a complete reversal of the flow direction (obtained when $\arctan(< w > / < u >) > 90°$) inside the separated region for the layers of the flow the closest to the wall.

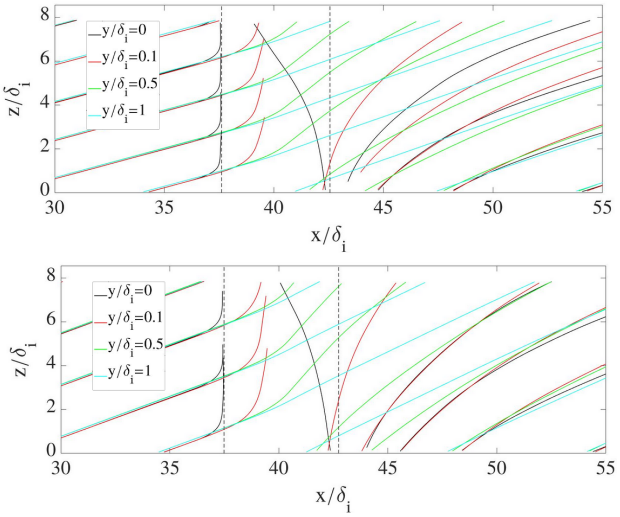

Figure 6: Streamlines for different wall-normal altitudes, ranging from the wall (skin-friction lines are plotted in that case) to $y = \delta_i$. Top : $\beta = 15°$, bottom : $\beta = 20°$

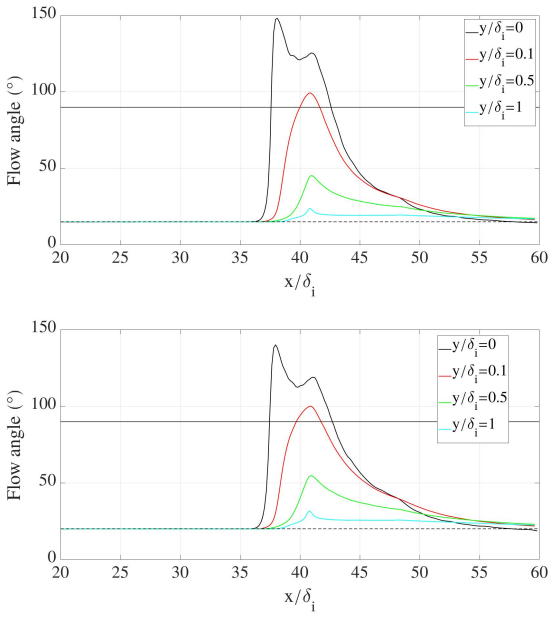

Figure 7: Flow angle with respect to x axis (given by $\arctan(< w > / < u >)$) for different wall-normal altitudes, ranging from the wall (angle of skin-friction lines are plotted in that case) to $y = \delta_i$. The horizontal full line situated at 90° allow to see where the flow is reversed. Horizontal dashed line shows the upstream imposed sweep. Top : $\beta = 15°$, bottom : $\beta = 20°$.

As seen on figure 4 (bottom), both the separation and reattachment points move (upstream and downstream respectively) when sweep is added. Moreover, the difference of L_{sep}

Table 3: Comparison between separation length and temperature upstream of interaction

β (°)	L_{sep}/δ_i	$T_w(x=35\delta_i)/T_\infty$
0	4.84	2.18
15	5.01	2.25
20	5.24	2.31

is greater between 20 and 15 degrees than the one seen between 0 and 15 degrees, despite a similar increase in wall temperature in both cases.

In addition to the effect on mean flow properties, it can be expected that the introduction of a sweep angle could also have an impact on the unsteady dynamics of the interaction. Figure 8 shows maps of spanwise-averaged Power Spectrum Densities (PSD) of wall pressure fluctuations. On the upper figure, the characteristic spectrum of a canonical unswept SBLI can be observed with low frequencies near the separation line. These frequencies are typically found to be two orders of magnitude below the ones associated with the upstream turbulent boundary layer. According to Piponniau *et al.* (2009), who developed a model for the low frequency unsteadiness of SBLI, a value of Strouhal $Stl_{Lsep} = f \cdot Lsep/U_\infty = 0.03$ should be observed for a flow with an upstream Mach number above 2. Downstream of the interaction, intermediate frequencies tend to dominate and are linked with shear layer vortices developing at the edge of the separation bubble. These observations are in line with several previous numerical and experimental studies (Dupont *et al.* (2006), Touber & Sandham (2009), Priebe & Martn (2012), Grilli *et al.* (2012)). When a spanwise velocity is added, peaks associated with higher frequencies appear near the average separation location. As seen on figure 8, values of Stl_{Lsep} of 0.1, 0.18 and 0.2 exhibits high energetic content. For $\beta = 20°$, we can moreover see a shift of the lowest-frequency peak from $Stl_{Lsep} = 0.03$ to $Stl_{Lsep} = 0.05$.

The intensity of the fluctuating pressure loads at the wall around the interaction area is also of particular importance in practical applications. To quantify this, we use a metric introduced by Grébert *et al.* (2018), defined as follows:

$$I'_{F_S}(x) = \frac{\sqrt{\langle F_S'^2 \rangle (x)}}{\langle F_S \rangle (x)} \text{ with } F_S(x,t) = \int_z P_w(x,z,t) ds \qquad (3)$$

Figure 9 shows the evolution of $I'_{F_S}(x)$ along x axis for the 3 sweep angles studied. It can be observed that adding a spanwise velocity component induces higher intensity of pressure loads, even though the maximum level presented here for the $\beta = 15°$ case is higher than the $\beta = 20°$ one right after the reflected shock (around $x/\delta_i = 38$). Further downstream, the higher the sweep angle, the higher the $I'_{F_S}(x)$. The effect of a crossflow is thus potentially detrimental for the structural loading of the surfaces involved in this type of configurations.

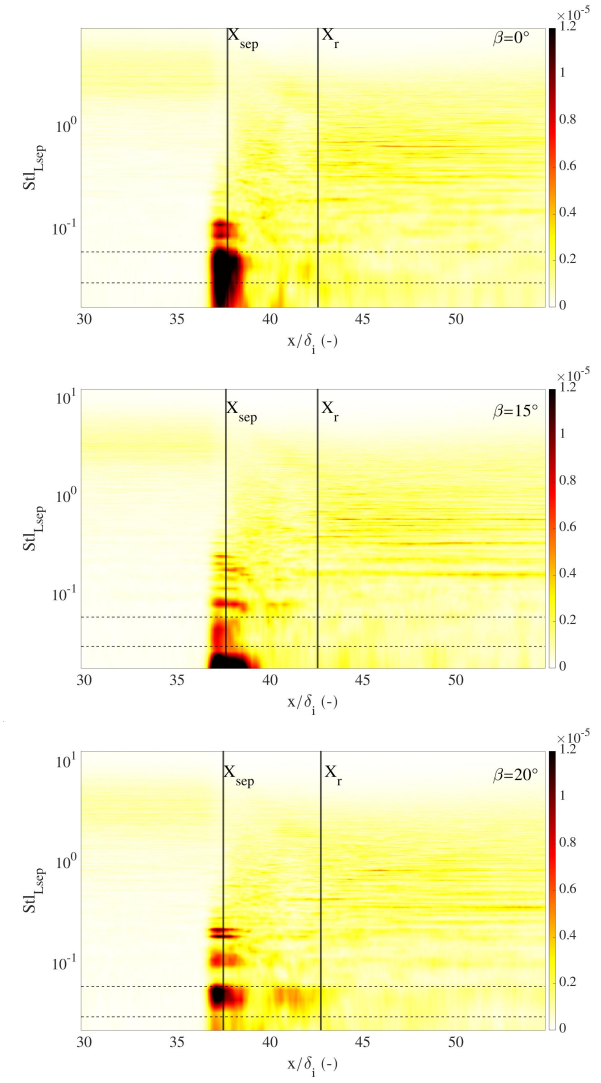

Figure 8: Spanwise-averaged PSD spectra of wall pressure fluctuations. From top to bottom : $\beta = 0°$, $\beta = 15°$, $\beta = 20°$. PSD are normalized by local integral $\int PSD(x,f)\,\mathrm{d}f$. x_{sep} and x_r stands for the mean locations of separation and reattachment respectively. The horizontal dashed lines are located at $Stl_{Lsep} = 0.03$ and $Stl_{Lsep} = 0.06$

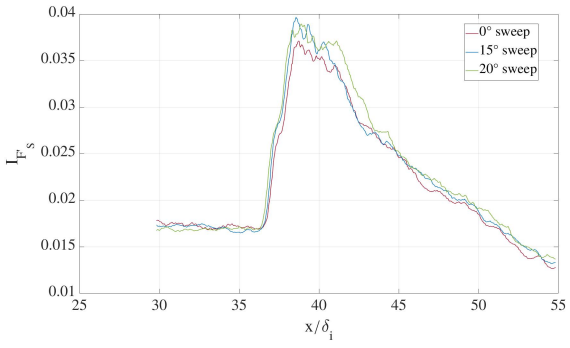

Figure 9: Streamwise evolution of the pressure loads intensity $I'_{F_S}(x)$ for the 3 sweep angles.

SUMMARY

In this work, several LES simulations have been conducted in order to compare swept and canonical shock/boundary layer interaction configurations. Results show that the sweep angle affect both the average flow and the unsteady low-frequency dynamics of the SBLI. The size of separated flow grows with the sweep angle, which can be linked to an increased wall temperature due to the added transverse velocity and the adiabatic nature of the wall. Around the separated bubble, the flow is highly skewed for the swept cases, which is favorable to the development of instabilities. It then gently recovers the expected post-shock direction. Pressure loads on the wall surface are higher for swept cases, which can be detrimental in real-life configurations such as supersonic air-intakes. The well-known unsteadiness of SBLI configurations is also altered by the presence of sweep, its characteristic low-frequency being slightly shifted to higher values.

ACKNOWLEDGEMENTS

This research was supported by the French Ministry of Defense through the financial support of the DGA (grant #2020-650026). This work was performed using resources from GENCI [CCRT-CINES-IDRIS] (Grant 2021-[A0102A07178] and 2022-[A0122A07178]).

REFERENCES

Bo, Wang, Weidong, Liu, Yuxin, Zhao, Xiaoqiang, Fan & Chao, Wang 2012 Experimental investigation of the micro-ramp based shock wave and turbulent boundary layer interaction control. *Physics of Fluids* **24** (5), 055110.

Clemens, Noel T & Narayanaswamy, Venkateswaran 2014 Low-frequency unsteadiness of shock wave/turbulent boundary layer interactions. *Annual Review of Fluid Mechanics* **46**, 469–492.

Dupont, P, Haddad, C & Debieve, JF 2006 Space and time organization in a shock-induced separated boundary layer. *Journal of fluid Mechanics* **559**, 255–277.

Grébert, Arnaud, Bodart, Julien, Jamme, Stéphane & Joly, Laurent 2018 Simulations of shock wave/turbulent boundary layer interaction with upstream micro vortex generators. *International Journal of Heat and Fluid Flow* **72**, 73–85.

Grilli, Muzio, Schmid, Peter J., Hickel, Stefan & Adams, Nikolaus A. 2012 Analysis of unsteady behaviour in shock-wave turbulent boundary layer interaction. *Journal of Fluid Mechanics* **700**, 1628.

Hopkins, Edward J & Inouye, Mamoru 1971 An evaluation of theories for predicting turbulent skin friction andheat transfer on flat plates at supersonic and hypersonic mach numbers. *AIAA JOURNAL* p. 20.

Klein, Markus, Sadiki, Amsini & Janicka, Johannes 2003 A digital filter based generation of inflow data for spatially developing direct numerical or large eddy simulations. *Journal of computational Physics* **186** (2), 652–665.

Lamouroux, Raphaël, Gressier, Jérémie & Grondin, Gilles 2016 A high-order compact limiter based on spatially weighted projections for the spectral volume and the spectral differences method. *Journal of Scientific Computing* **67** (1), 375–403.

Larsson, Johan, Kumar, Vedant, Oberoi, Nikhil, Renzo, Mario Di & Pirozzoli, Sergio 2022 Large-eddy simulations of idealized shock/boundary-layer interactions with cross-flow. *AIAA Journal* pp. 1–13.

Liu, Yen, Vinokur, Marcel & Wang, Zhi Jian 2006 Spectral difference method for unstructured grids i: Basic formulation. *Journal of Computational Physics* **216** (2), 780–801.

Padmanabhan, Sathyan, Maldonado, Jorge C, Threadgill, James AS & Little, Jesse C 2021 Experimental study of swept impinging oblique shock/boundary-layer interactions. *AIAA journal* **59** (1), 140–149.

Piponniau, S., Dussauge, J. P., Debive, J. F. & Dupont, P. 2009 A simple model for low-frequency unsteadiness in shock-induced separation. *Journal of Fluid Mechanics* **629**, 87108.

Priebe, Stephan & Martn, M. Pino 2012 Low-frequency unsteadiness in shock waveturbulent boundary layer interaction. *Journal of Fluid Mechanics* **699**, 149.

Touber, Emile & Sandham, Neil D 2009 Large-eddy simulation of low-frequency unsteadiness in a turbulent shock-induced separation bubble. *Theoretical and Computational Fluid Dynamics* **23** (2), 79–107.

Van Driest, Edward R 1956 On turbulent flow near a wall. *Journal of the aeronautical sciences* **23** (11), 1007–1011.

Xie, Zheng-Tong & Castro, Ian P 2008 Efficient generation of inflow conditions for large eddy simulation of street-scale flows. *Flow, turbulence and combustion* **81** (3), 449–470.